https://doi.org/10.5194/egusphere-2026-3946
Preprint. Discussion started: 28 July 2026

Cold-stage system for Impact-initiated Contact freezing Experiments (C-ICE)

Jingchuan Chen[1], Upasna B. Rai[1], Kyle A. McMillan[2,3], Ryan D. Davis[4,5], Margaret A. Tolbert[2,3], and Sarah D. Brooks[1*]

[1] Department of Atmospheric Sciences, Texas A&M University, College Station, Texas 77843, USA
[2] Cooperative Institute for Research in Environmental Sciences, University of Colorado, Boulder, Boulder, Colorado 80309, USA
[3] Department of Chemistry, University of Colorado, Boulder, Boulder, Colorado 80309, USA
[4] Sandia National Laboratories, Albuquerque, New Mexico 87123, USA
[5] Department of Chemistry and Chemical Biology, University of New Mexico, Albuquerque, New Mexico 87131, USA

Correspondence to: Sarah D. Brooks (sbrooks@tamu.edu)

Abstract. Ice nucleation by atmospheric aerosols plays a central role in cloud microphysical processes, exerting strong influences on Earth's radiation balance and precipitation formation. Among heterogeneous ice nucleation pathways, contact freezing induced by aerosol-droplet collisions remains one of the least quantitatively constrained, largely due to the scarcity of experimental approaches capable of directly probing impact-initiated freezing under controlled and reproducible conditions. Here we present the Cold-stage system for Impact-initiated Contact freezing Experiments (C-ICE), a laboratory system developed to enable controlled, repeatable, and size-resolved investigation of contact freezing triggered by particle-droplet collisions. C-ICE combines a fixed supercooled droplet with a precisely conditioned aerosol jet, allowing particle size, number concentration, collision geometry, and thermodynamic state to be independently characterized and experimentally constrained. At the single-droplet level, freezing onset is identified using complementary optical criteria based on breath figure formation and grayscale analysis. Application of C-ICE to silver iodide aerosols reveals sharp frozen fraction transitions over narrow temperature intervals (≈2 °C), with median freezing temperatures shifting systematically toward higher values from -12.6 °C for 200 nm particles to -12.0 °C for 800 nm particles, and to -10.1 °C for the polydisperse aerosol. By integrating a theoretical collision model with experimentally determined collision efficiencies, we constrain the collision efficiency of the C-ICE system, enabling measured aerosol concentrations to be converted into effective particle collision rates onto the droplet. This novel C-ICE system provides a robust method for quantifying impact-initiated contact freezing and advances process-level understanding of contact freezing in clouds.

1 Introduction

Ice nucleation triggered by atmospheric aerosol particles plays a key role in cloud microphysical processes by regulating cloud formation and development, further influencing radiative forcing and precipitation (Kanji et al., 2017; Knopf and Alpert, 2023;

https://doi.org/10.5194/egusphere-2026-3946
Preprint. Discussion started: 28 July 2026

Chen et al., 2024). Ice nucleating particles (INPs) can initiate ice formation through several heterogeneous nucleation pathways, including immersion freezing, contact freezing, deposition freezing, and condensation freezing (Murray et al., 2012; Knopf and Koop, 2006; Lohmann et al., 2016). Among these pathways, contact freezing refers to ice formation that occurs when an aerosol particle comes into contact with a supercooled liquid droplet or when nucleation is initiated at the air-liquid-particle triple interface (Vali et al., 2015). Contact freezing has been reported to be more efficient than immersion or deposition freezing (Pitter and Pruppacher, 1973; Hoose and Mohler, 2012; Fornea et al., 2009; Brooks et al., 2014; Hoffmann et al., 2013a; Collier and Brooks, 2016). However, the quantitative differences between contact and immersion freezing temperatures vary widely, with some studies reporting negligible differences (Nagare et al., 2016; Matthews et al., 2023). As a result, the overall contribution of contact freezing to atmospheric ice formation remains poorly constrained (Ladino Moreno et al., 2013; Burrows et al., 2022; Zhang et al., 2024).

Over the past several decades, the physical basis for contact nucleation has been debated. A key question is whether nucleation is triggered by the force of particle-droplet collision or by the presence of a particle at the droplet-air interface (Fletcher, 1969; Cooper, 1974; Durant and Shaw, 2005; Shaw et al., 2005; Fornea et al., 2009). In many cold-stage experiments, particles are intentionally placed in contact with droplet edge, or evaporation is used to bring immersed particles into contact with the interface (Durant and Shaw, 2005; Schiffman et al., 2025). These experiments are collectively referred to as surface-initiated contact freezing. While such studies provide important insight into interfacial nucleation processes, they do not directly address how particle-droplet collisions influence ice nucleation.

In contrast, if the physical basis for nucleation is the particle-droplet collision event, the nucleation event may be influenced by collision dynamics, including particle size and relative velocity or pressure perturbations generated by the collision (Hoffmann et al., 2013a; Yang et al., 2019). This process is referred to here as impact-initiated contact freezing. Despite its potential importance, the role of collisions in initiating freezing remains difficult to isolate experimentally, as most existing approaches do not explicitly control or quantify particle-droplet collision processes (Ladino Moreno et al., 2013). An experimental method capable of directly probing collision occurrence and its influence on freezing temperature is therefore needed.

A wide range of experimental approaches has been employed to study contact freezing, including wind tunnels (Pitter and Pruppacher, 1973; Diehl et al., 2002), electrodynamic balance (EDB) systems (Svensson et al., 2009; Hoffmann et al., 2013b), mixing cloud chambers (Langer et al., 1978; DeMott, 1995), and continuous flow cloud chambers (Schaller and Fukuta, 1979; Ladino et al., 2011b). In these systems, particle-droplet interactions typically arise from transport-driven processes such as diffusion, sedimentation, or turbulent mixing. Collision probability is not directly controlled and is often inferred indirectly from freezing statistics (Ladino et al., 2011a; Nagare et al., 2015). Therefore, measured freezing efficiencies reflect a convolution of collision processes and intrinsic nucleation activity, which complicates mechanistic interpretation. Consequently, the significance of the collision remains uncertain.

From a theoretical perspective, the calculation of collision efficiency is straightforward and depends on multiple transport mechanisms, including Brownian motion, inertial impaction, interception, thermophoresis, diffusiophoresis, and electric forces

https://doi.org/10.5194/egusphere-2026-3946
Preprint. Discussion started: 28 July 2026

(Pruppacher and Klett, 2010). Classical collision theory predicts a pronounced minimum in collision efficiency for submicron aerosol particles (typically ~0.1-1 μm) collected by droplets, known as the Greenfield gap. In this regime, particles are too large for efficient diffusive transport yet too small for inertial collection (Greenfield, 1957; Ladino et al., 2011a). Many particles known to act as atmospheric INPs occur within this size range, causing particle sizes associated with efficient ice nucleation to overlap with those associated with inefficient particle-droplet collision. Consequently, the number of effective particle-droplet collisions may be limited, complicating the interpretation of contact freezing measurements when collision processes are not explicitly constrained.

Here we introduce Cold-stage system for Impact-initiated Contact freezing Experiments (C-ICE), a laboratory system designed to quantify impact-initiated contact freezing under controlled conditions. C-ICE combines a fixed supercooled droplet with a conditioned aerosol jet, enabling directed and repeatable particle-droplet collisions. Aerosol size, number concentration, and thermodynamic state are independently characterized. Freezing onset is identified at the single-droplet level using complementary optical criteria based on breath figure formation and grayscale analysis. Breath figures refer to the condensation patterns of water vapor that form on a surface cooled below the ambient dew point (Baker, 1922; Beysens and Knobler, 1986; Bouillant et al., 2025). In addition, we provide a theoretically based collision model to quantify C-ICE measurements. In this study, we apply C-ICE to silver iodide (AgI) aerosols to demonstrate its capability to resolve size-dependent freezing behavior and to experimentally constrain collision efficiency under well-defined conditions. The C-ICE system developed here provides experimentally constrained insight into particle-droplet interactions and offers a potential pathway for improving the representation of contact freezing in atmospheric models.

2 Methods

2.1 Overview of the C-ICE experimental setup

The Cold-stage system for Impact-initiated Contact freezing Experiments (C-ICE) was developed to enable direct and repeatable aerosol-droplet collisions under well-defined thermodynamic and flow conditions. The overall design of the system is illustrated schematically in Fig. 1a, with a corresponding flow schematic shown in Fig. 1b. The symbols used throughout this study are summarized in Table A1. This experimental setup integrates aerosol generation, environmental conditioning, controlled particle-droplet impact, and optical detection of freezing. The C-ICE system provides flexibility to investigate impact-initiated contact freezing across different particle types, particle sizes, flow rates, and collision conditions.

https://doi.org/10.5194/egusphere-2026-3946
Preprint. Discussion started: 28 July 2026

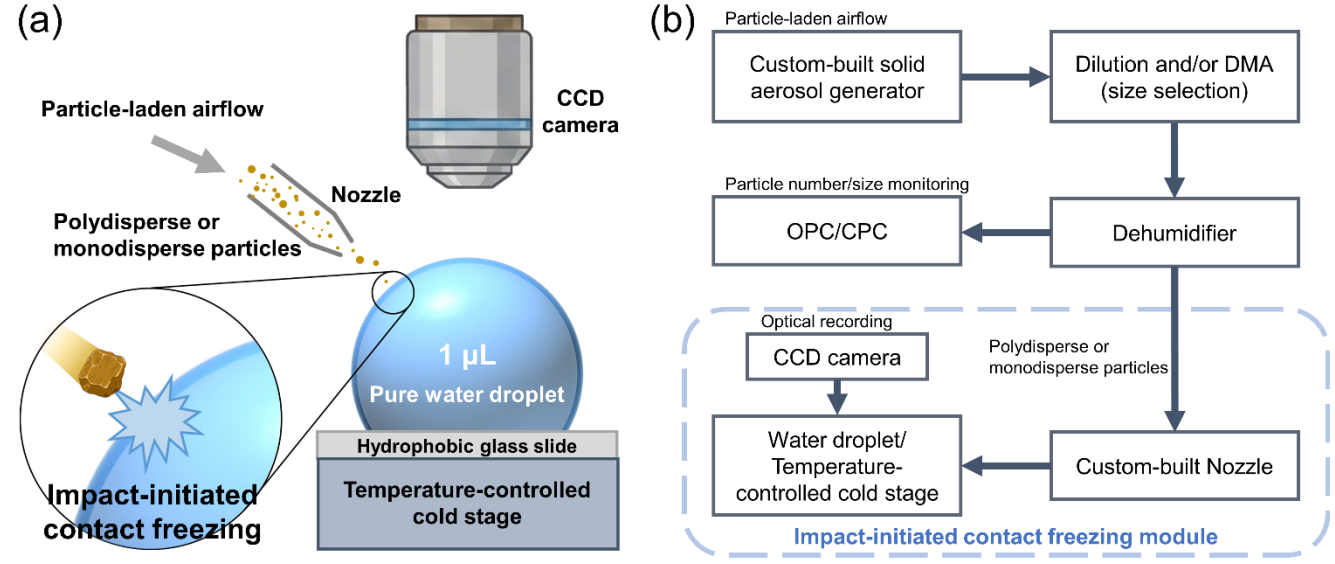

Figure 1: Schematic of the Cold-stage system for Impact-initiated Contact freezing Experiments (C-ICE). (a) Conceptual illustration of impact-initiated contact freezing. (b) Flow schematic of the C-ICE system. Aerosols are generated using a custom-built solid aerosol generator with nitrogen as the carrier gas, followed by dilution and/or size selection using a differential mobility analyzer (DMA). The aerosol stream then passes through a dehumidifier, which removes excess water vapor and stabilizes thermodynamic conditions before the stream enters the cold-stage region. Particle number concentration and size distribution are monitored using a condensation particle counter (CPC) and an optical particle counter (OPC). The conditioned aerosol is delivered through a custom-designed nozzle to collide with a supercooled pure-water droplet placed on a hydrophobic glass substrate mounted on a temperature-controlled cold stage. Freezing is triggered upon particle-droplet impact and recorded using a CCD camera.

A custom-built solid aerosol generator is used to produce a stable particle-laden airflow. The generated aerosol is subsequently conditioned through dilution and/or size selection, allowing either polydisperse or monodisperse particle populations to be delivered. Dilution is used to adjust particle number concentration, while size selection isolates particles within a defined size range for targeted experiments. For size-selected experiments, a differential mobility analyzer (DMA, model 3080, TSI Inc., USA) is used to size-select aerosol particles with diameters up to 1.0 µm. Following size selection, the aerosol flow is dehumidified to remove excess water vapor and thermally conditioned using a double-jacketed flow tube. Temperature control is achieved using a recirculating chiller (NESLAB ULT-80, Thermo Electron Inc., USA) with ethanol as the coolant, allowing both the aerosol particles and the nitrogen carrier gas to equilibrate to the target temperature prior to collision. This conditioning step minimizes unintended condensation in the collision region and ensures reproducible experimental conditions. Conditioned aerosol particles are directed toward a single supercooled pure-water droplet (1 µL, UHPLC grade, Sigma-Aldrich Inc., USA) pipetted on an Aquasil-treated hydrophobic glass substrate mounted on a temperature-controlled cold stage (model LTS350, Linkam Inc., UK) (Fornea et al., 2009). The aerosol is delivered through a custom-designed nozzle, which defines the collision geometry and velocity. The nozzle geometry and flow conditions are adjustable, enabling investigation of impact-initiated contact freezing under different collision regimes. In this work, a nozzle orifice diameter of 0.8 mm, an aerosol flow rate of

https://doi.org/10.5194/egusphere-2026-3946
Preprint. Discussion started: 28 July 2026

120 cm^3 min^{-1}, and a corresponding jet velocity of 4.0 m s^{-1} were employed. This configuration ensures efficient particle delivery to the target droplet, while the associated collision efficiency is quantified and discussed in Sects. 2.3 and 3.3.

Particle number concentrations and size distributions downstream of the conditioning unit are monitored in real time using a condensation particle counter (CPC, model 3075, TSI Inc., USA) and/or an optical particle counter (OPC, model 1.108, GRIMM Inc., Germany), ensuring that the monodisperse and/or polydisperse particle populations delivered to the target droplet are well characterized. The cold stage is cooled at a rate of 1 °C min^{-1}, while a charge-coupled device (CCD) camera mounted on an optical microscope system (BX51M equipped with a 5x objective lens, Olympus Inc., Japan) continuously records the droplet during cooling, capturing the entire contact freezing process. Once the droplet has fully frozen, the cooling program and image acquisition are terminated, marking the completion of a single experimental run. The cold stage is then allowed to return to room temperature, after which a new pure-water droplet (1 µL) is pipetted onto a freshly cleaned hydrophobic glass substrate to initiate the next measurement. Solid aerosol particles are used as experimental samples; in this study, silver iodide (AgI, 99.9% metals basis, Thermo Scientific Alfa Aesar) is employed as a representative test material. Each experimental condition was repeated 30-50 times to ensure statistical robustness of the derived frozen fraction and freezing temperatures. By combining controlled aerosol-droplet collisions with precise temperature regulation and optical detection, C-ICE provides a quantitative experimental approach to investigate impact-initiated contact freezing and to constrain the freezing efficiency of different INPs under controlled conditions.

2.2 Calculation of frozen fraction and uncertainty estimation

Each experiment in C-ICE employs a single freshly pipetted pure-water droplet, and experiments are repeated multiple times under identical conditions. Accordingly, the freezing of each droplet and its associated freezing temperature are treated as independent realizations of the same stochastic nucleation process. The total number of droplets (N_{tot}) therefore corresponds to the number of repeated experiments conducted for a given set of conditions.

Consistent with common treatments of heterogeneous ice nucleation, we assume that contact freezing is promoted by a finite number of active sites on the surface of INPs. Under the singular description of nucleation, the probability of freezing is assumed to depend solely on temperature, while time is treated as an implicit experimental parameter determined by the prescribed cooling protocol (Vali et al., 2015; Niedermeier et al., 2011). The frozen fraction at temperature T, $f_{ice}(T)$, defined as the fraction of droplets that have frozen at temperatures warmer than or equal to T, is given by (Vali, 1971)

$$f_{ice}(T) = \frac{N_f(T)}{N_{\mathrm{tot}}} \quad (1)$$

where $N_f(T)$ is the cumulative number of droplets that have frozen at temperatures warmer than or equal to T, and N_{tot} is the total number of droplets measured under a given experimental condition.

To construct $f_{ice}(T)$, the measured freezing temperatures from repeated experiments were first sorted from warmest to coldest. The frozen fraction was then evaluated on a discrete temperature grid spanning the observed freezing temperature range. Unless otherwise stated, the grid spacing ΔT was selected adaptively to provide sufficient resolution while maintaining smooth and

https://doi.org/10.5194/egusphere-2026-3946
Preprint. Discussion started: 28 July 2026

interpretable frozen fraction curves. Specifically, ΔT was constrained to be no smaller than 0.1 ℃ and to be an integer multiple of 0.1 ℃, and was chosen to yield at least 10 grid points across the temperature range whenever possible.

Uncertainty in the frozen fraction was quantified using the Wilson score interval for a binomial proportion, which provides robust confidence intervals even for small sample sizes or proportions close to 0 or 1 (McCluskey et al., 2018; Gong et al., 2020). This approach avoids the known limitations of the normal approximation and is therefore well suited for frozen fraction analyses in this study (Agresti and Coull, 1998).

For a given temperature T, the Wilson score interval for $f_{ice}(T)$ at a specified confidence level is given by (Wilson, 1927)

$$\frac{f_{\mathrm{ice}} + \frac{z^2}{2N_{tot}} \pm z\sqrt{\frac{f_{\mathrm{ice}}(1-f_{\mathrm{ice}})}{N_{tot}} + \frac{z^2}{4N_{tot}^2}}}{1+\frac{z^2}{N_{tot}}} \tag{2}$$

where z is the critical value of the standard normal distribution corresponding to the desired confidence level, e.g., $z = 1.96$ for a 95% confidence interval.

The characteristic median freezing temperature, T_{50}, is defined as the temperature at which $f_{ice}(T) = 0.5$, and is obtained by linear interpolation between adjacent grid points on the frozen fraction curve. Note that the reported T_{50} may differ slightly from the median of the measured freezing temperatures due to discretization and interpolation, typically by 0.1 ℃ (Table S1). This difference is smaller than the instrumental temperature uncertainty of the cold stage (± 0.2 ℃) and does not affect the interpretation of the results. Both definitions are therefore effectively equivalent within experimental uncertainty.

The frozen fraction analysis adopted here is consistent with methodologies widely used in previous heterogeneous ice nucleation studies (Zhang et al., 2022; Creamean et al., 2025; DeMott et al., 2025). By expressing freezing behavior in terms of $f_{ice}(T)$, ice nucleation activity can be quantified in a manner that facilitates direct comparison across different nucleation modes, particle types, and experimental platforms.

2.3 Collision model and contributing physical mechanisms

To quantify collision probabilities in the C-ICE system, we developed a particle-droplet collision model tailored to the dimensions and flow conditions of the C-ICE apparatus. In this study, the instrumental collision efficiency (CE) is defined as the fraction of particles entering the nozzle jet that physically collide with the droplet under the prescribed experimental flow and thermodynamic conditions. Operationally, CE is calculated as the ratio of the colliding particle flux to the total particle flux transported by the nozzle jet.

Particle transport and collection, and hence collision efficiency, are governed by particle physicochemical properties and the surrounding flow field (Pruppacher and Klett, 2010; Ladino Moreno et al., 2013). Brownian motion dominates the collection of small particles, whereas inertial impaction and interception primarily govern collisions for larger particles (Slinn, 1977; Jung and Lee, 1998; Park et al., 2005). In addition, thermophoresis, diffusiophoresis, and electric forces may contribute significantly to particle-droplet collisions when temperature gradients, vapor concentration gradients, or particle charging are

https://doi.org/10.5194/egusphere-2026-3946
Preprint. Discussion started: 28 July 2026

present, respectively (Davenport and Peters, 1978; Andronache et al., 2006). Together, these six physical mechanisms act concurrently to determine the total collision efficiency. Accordingly, the total instrumental collision efficiency, CE, is expressed using an independent additive formulation:

$$CE = E_{Br} + E_{Imp} + E_{Int} + E_{\mathrm{Th}} + E_{Df} + E_E \tag{3}$$

where E_{Br}, E_{Imp}, E_{Int}, E_{Th}, E_{Df}, and E_E represent the contributions from Brownian motion, inertial impaction, interception, thermophoresis, diffusiophoresis, and electric forces, respectively.

Specifically, the collision efficiency due to Brownian motion, E_{Br}, is calculated following Jung and Lee (1998), which is given by

$$E_{Br} = 2\left(\frac{\sqrt{3}\pi}{4Pe}\right)^{2/3}\left[\frac{(1-\alpha)(3\sigma+4)}{J+\sigma K}\right]^{1/3} \tag{4}$$

where α is the packing density, defined as the volume fraction of droplets. In the present experiments, particle-droplet interactions are treated in the single-target-droplet limit, where a single stationary droplet is present as the collision target. Therefore, droplet-droplet interactions are absent and the droplet packing density α is set to zero. Under this condition, following Park et al. (2005), the group parameters J and K both reduce to unity. The parameter σ is the viscosity ratio of water to air, and Pe is the Peclet number, defined as $Pe = D_{\mathrm{d}}U/D_{\mathrm{diff}}$, where D_{d} is the droplet diameter, U is the particle approach velocity at the moment of particle-droplet collision, and D_{diff} is the particle diffusion coefficient, given by $D_{\mathrm{diff}} = k_{\mathrm{B}}T_aC_{\mathrm{c}}/(3\pi\mu d_{\mathrm{p}})$. Here, k_{B} is the Boltzmann constant, T_a is the absolute temperature of air, μ is the air viscosity, d_{p} is the particle diameter, and C_{c} is the Cunningham slip correction factor, represented by

$$C_{\mathrm{c}} = 1 + 2.493\frac{\lambda}{d_{\mathrm{p}}} + 0.84\frac{\lambda}{d_{\mathrm{p}}}\exp\left(-0.435\frac{d_{\mathrm{p}}}{\lambda}\right) \tag{5}$$

where λ is the mean free path of air molecules.

For larger particles, inertial impaction becomes the dominant particle collection mechanism. The collision efficiency due to inertial impaction (E_{Imp}) is given following Calvert (1984) as

$$E_{Imp} = \left(\frac{Stk}{Stk+0.35}\right)^2 \tag{6}$$

where Stk is the Stokes number, a dimensionless number characterizing the inertial response of particles relative to the carrier flow, defined as

$$Stk = \frac{\rho_{\mathrm{p}}d_{\mathrm{p}}^2U}{18\mu D_{\mathrm{d}}} \tag{7}$$

with ρ_{p} denoting the particle density.

https://doi.org/10.5194/egusphere-2026-3946
Preprint. Discussion started: 28 July 2026

Interception refers to the collection of particles that largely follow the airflow streamlines around the droplet but are captured when their finite size brings them into contact with the droplet surface, and it is more effective for larger particles. Following Jung and Lee (1998), the collision efficiency contribution due to interception (E_{Int}) is described as

$$E_{Int} = \frac{1-\alpha}{J+\sigma K}\left\{\frac{R}{1+R} + \frac{1}{2}\left(\frac{R}{1+R}\right)^2 (3\sigma+4)\right\} \tag{8}$$

where $R = d_{\mathrm{p}}/D_{\mathrm{d}}$.

Thermophoresis arises when a temperature gradient exists between the particle-laden airflow and the droplet surface, driving particles toward the colder region. Under such conditions, the collision efficiency contribution due to thermophoresis (E_{Th}) is calculated following Andronache et al. (2006)

$$E_{\mathrm{Th}} = \frac{4\alpha_{Th}\left(2 + 0.6R_e^{1/2}P_r^{1/3}\right)(T_a - T_s)}{UD_d} \tag{9}$$

where T_a and T_s are the absolute temperatures of air and droplet surface, respectively. R_e is the droplet Reynolds number, P_r is the Prandtl number for air, and α_{Th} is the thermophoretic transport coefficient defined following Eq. (A3) in Andronache et al. (2006).

Diffusiophoresis contributes to particle-droplet collisions when gradients in water vapor concentration are present near the droplet surface, typically under subsaturated or weakly supersaturated conditions. The collision efficiency due to diffusiophoresis (E_{Df}) is given by (Andronache et al., 2006)

$$E_{Df} = \frac{4\beta\left(2 + 0.6R_e^{1/2}S_{c_w}^{1/3}\right)\left(\frac{p_s^0}{T_s} - \frac{p_a^0 \mathrm{RH}}{T_a}\right)}{UD_d} \tag{10}$$

where S_{c_w} is the Schmidt number of water vapor in air, RH is the ambient relative humidity. p_a^0 and p_s^0 are water vapor pressure at temperatures T_a and T_s, and the coefficient β is given by Eq. (A4) in Andronache et al. (2006).

Electric forces, also referred to as electroscavenging, may enhance particle-droplet collisions when particles carry net electric charge or when electric fields are present. Following Andronache et al. (2006), the collision efficiency contribution due to electric forces (E_E) is expressed as

$$E_E = \frac{16KC_c a^2 {\alpha_q}^2 d_p}{3\pi\mu U} \tag{11}$$

where K is the Coulomb constant, α_q is an empirical parameter characterizing particle charging, and $a = 0.83 \times 10^{-6}$.

Overall, Brownian motion, inertial impaction, interception, thermophoresis, diffusiophoresis, and electric forces jointly determine the total instrumental collision efficiency, which is constrained to the physically meaningful range between 0 and 1. Importantly, the CE discussed throughout this study characterizes the C-ICE instrumental configuration, namely a particle-laden nozzle jet impinging on a supercooled droplet, and should not be interpreted as an atmospheric collision efficiency. Unless otherwise specified, the term collision efficiency refers exclusively to this instrumental particle-droplet CE. Under the controlled laboratory conditions of C-ICE, such particle-droplet collisions are theoretically predictable and experimentally

https://doi.org/10.5194/egusphere-2026-3946
Preprint. Discussion started: 28 July 2026

controllable and repeatable, as demonstrated in the Results section below. This approach provides a foundation for interpreting impact-initiated contact freezing measurements and for guiding future efforts to parameterize contact freezing in atmospheric models.

3 Results and Discussion

3.1 Identification of impact-initiated contact freezing in C-ICE

Impact-initiated contact freezing requires that ice nucleation be triggered at the moment of physical contact between an aerosol particle and a supercooled droplet. Accurate identification of the freezing moment is therefore essential for determining the corresponding freezing temperature and for distinguishing contact freezing from other heterogeneous nucleation modes. In the C-ICE system, freezing events are identified optically using two complementary and independent criteria: (i) the onset of freezing is primarily identified by the appearance of breath figures (described below), and (ii) complete freezing is determined from abrupt changes in the grayscale value of the droplet.

Figure 2 illustrates these optical signatures for a representative experiment with 200 nm AgI particles as the contact nuclei. In Fig. 2a, freezing is monitored using the grayscale value of the droplet, calculated from the mean pixel intensity within a fixed central droplet region shown in Fig. S1. Grayscale values range from 0 (black) to 255 (white), with larger values corresponding to brighter images (Budke and Koop, 2015). Representative optical images corresponding to different stages of the experiment are shown in Figs. 2b-2e, with black arrows linking each image to its corresponding temperature in Fig. 2a. While the droplet remains in the supercooled liquid state (Figs. 2b and 2c), the droplet grayscale is nearly constant. A slight increase in grayscale at -11.4 ℃ corresponds to the introduction of aerosol stream, which induces minor droplet oscillations or deformations without freezing. At the onset freezing temperature (-12.2 ℃; red dashed line; Fig. 2d), a small but detectable decrease in grayscale occurs, preceding the much larger and abrupt change associated with complete freezing at -12.4 ℃ (blue dashed line; Fig. 2e). The transient brightening observed immediately before complete freezing is attributed to an optical effect during rapid ice propagation through the droplet. The shaded inset highlights the subtle grayscale response, demonstrating that the onset freezing temperature can, in principle, be identified from grayscale analysis alone. Throughout this study, the onset freezing temperature refers specifically to the temperature at which freezing is initiated in an individual droplet as a direct consequence of an aerosol-droplet collision. This definition differs from that used in many previous studies, where “onset” often indicates the highest temperature at which the first droplet freezes within an ensemble (i.e., the first non-zero point on a frozen fraction curve) (Hoose and Mohler, 2012; Murray et al., 2012; Schill et al., 2014; Alsante et al., 2024).

https://doi.org/10.5194/egusphere-2026-3946
Preprint. Discussion started: 28 July 2026

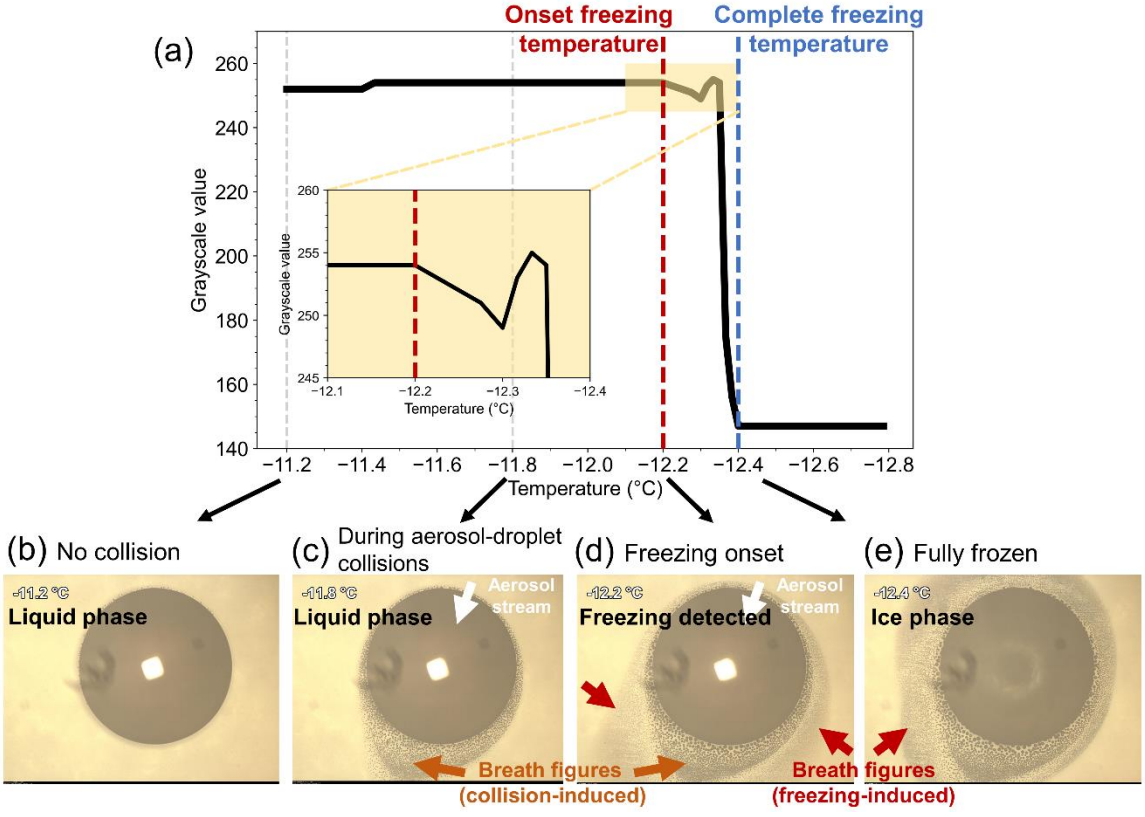

Figure 2: Optical identification of impact-initiated contact freezing in the C-ICE system. (a) Evolution of the grayscale value of a single supercooled pure-water droplet as a function of temperature during an impact-initiated contact freezing experiment with 200 nm silver iodide (AgI) particles. The onset freezing temperature is indicated by the red dashed line, while the complete freezing temperature is marked by the blue dashed line. The shaded inset highlights the sensitivity of the grayscale signal to the onset freezing event. Representative optical images illustrating the evolution of the droplet during the experiment are shown in panels (b-e), with the corresponding temperatures indicated in the upper-left corner of each image and linked to panel (a) by black arrows. (b) Supercooled liquid droplet before introduction of the aerosol stream (-11.2 °C). (c) Liquid droplet during aerosol-droplet collisions, showing localized breath figures associated with collision-induced vapor saturation in the wake region of the droplet (-11.8 °C). (d) Onset of contact freezing, marked by the appearance of pronounced breath figures associated with freezing-induced thermal and vapor perturbations (-12.2 °C). (e) Fully frozen droplet (ice phase; -12.4 °C). The two types of breath figures highlighted in panels (c–e) represent distinct physical processes: those marked in orange arise from collision-induced vapor fields, whereas those marked in red indicate condensation patterns generated by latent heat release during freezing. White arrows indicate the direction of the aerosol stream. The image region used for grayscale analysis is shown in Fig. S1. The complete freezing process is provided in Movie S1. The onset freezing temperature is defined as the temperature at which freezing is initiated in an individual supercooled droplet as a direct consequence of an aerosol-droplet collision and is distinct from ensemble-based onset definitions commonly used in frozen fraction analyses.

Breath figures provide a visually distinct and physically meaningful indicator of freezing onset. Breath figures refer to the condensation patterns of water vapor that form on a surface cooled below the ambient dew point (Baker, 1922; Beysens and Knobler, 1986; Bouillant et al., 2025). In the C-ICE system, they serve as a sensitive optical signal associated with local thermal and vapor perturbations following particle-droplet interaction. Prior to freezing (Fig 2c), a locally saturated vapor region forms on the leeward side of the droplet due to the aerosol stream impinging on the droplet coming from the upper-

https://doi.org/10.5194/egusphere-2026-3946
Preprint. Discussion started: 28 July 2026

right direction in the field of view (white arrow). Water vapor condenses onto the slightly cooler hydrophobic glass substrate in this region, producing localized breath figures that indicate ongoing aerosol-droplet interactions. These collision-induced breath figures are highlighted by the orange annotations in Fig. 2. At the onset freezing temperature (-12.2 °C; Fig. 2d), a second type of breath figure appears abruptly around the droplet perimeter, forming a distinct condensation ring highlighted by the red annotations. This newly formed condensation pattern signals the initiation of impact-initiated contact freezing. A direct comparison between conditions immediately before freezing and at freezing onset is provided in Fig. S2. Collision-induced breath figures are already present at -12.1 °C during ongoing aerosol-droplet collisions, whereas the freezing-induced condensation ring first appears at -12.2 °C. This comparison demonstrates that the secondary breath-figure pattern is specifically associated with freezing initiation rather than with aerosol-droplet collisions alone. When freezing is triggered at the particle-droplet contact site, the liquid-to-ice phase transition releases latent heat (Pruppacher and Klett, 2010; Harrison et al., 2018). The resulting local perturbation of temperature and vapor fields (Biswas et al., 2025; Hazra et al., 2022) enhances evaporation from the droplet surface and drives rapid condensation on the surrounding substrate. As freezing progresses, the droplet transitions into a fully frozen ice phase (Fig. 2e). At this stage, the aerosol stream has already been terminated, and the subsequent bulk solidification of the droplet releases additional latent heat, producing a broader condensation pattern. Because the experimental cell is maintained under subsaturated conditions, these newly formed breath figures evaporate rapidly and disappear within a short time. The complete freezing process is provided in the Supplement (Movie S1). In the present experiments, breath figure formation is transient and spatially localized, only at the droplet surface rather than by large-scale environmental cooling. This is an indication that condensation is locally induced by latent heat release associated with contact freezing. As a result, breath figures provide a sensitive and physically meaningful optical signature of the onset of contact freezing, directly linked to the initiation of the phase transition.

The use of onset freezing temperature is physically motivated. In immersion or deposition freezing experiments, grayscale-based analyses typically identify the temperature of complete freezing, which reflects bulk solidification of the droplets and is appropriate when nucleation occurs throughout the liquid or vapor phase (Kiselev et al., 2017; Thornton et al., 2023; Thompson et al., 2025). In contrast, contact freezing is initiated at a localized site, such as the solid-liquid-air contact line or a region experiencing a pressure perturbation during particle impact (Yang et al., 2019; Rosky et al., 2023). Once ice formation is triggered, subsequent freezing of the bulk droplet proceeds spontaneously through rapid ice propagation. According to classical descriptions of contact nucleation, the initial nucleation event determines the freezing outcome, whereas the subsequent ice growth is governed by thermodynamic and kinetic processes that no longer depend on the triggering mechanism (Pruppacher and Klett, 2010; Ladino Moreno et al., 2013; Wang et al., 2021; Kalita et al., 2023; Chu et al., 2024). In principle, the temperature of complete freezing is not required to be lower than the onset freezing temperature. In practice, however, the cold stage is operated at a constant cooling rate, leading to experimentally observed complete freezing temperatures that are systematically slightly lower than the onset freezing temperatures. For the representative case of 200 nm AgI particles shown in Fig. 2a, the difference between onset and complete freezing temperatures is only 0.2 °C. Statistical analyses of both monodisperse and polydisperse particles further indicate that this temperature difference is consistently within 0.2-0.3 °C

https://doi.org/10.5194/egusphere-2026-3946
Preprint. Discussion started: 28 July 2026

(Table S1), comparable to instrumental temperature uncertainty. Therefore, the onset freezing temperature provides a more physically meaningful representation of the nucleation condition for impact-initiated contact freezing.

In this study, breath figure detection provides the primary operational criterion for identifying freezing onset at the single-droplet level, while grayscale analysis provides an independent consistency check. This dual-criterion approach enables a physically grounded definition of freezing temperature for impact-initiated contact freezing and establishes the basis for subsequent frozen fraction analysis.

3.2 System performance and background freezing behavior

The performance and reliability of the C-ICE system were evaluated through a combination of background freezing measurements, repeated impact-initiated contact freezing experiments, and simulations of the aerosol conditioning unit. Together, these analyses establish the experimental credibility of the system, quantify the intrinsic background freezing behavior in the absence of particles, and demonstrate that thermodynamic and flow conditions relevant to aerosol-droplet collisions are well controlled and reproducible.

Figure 3 provides an assessment of experimental repeatability and background freezing behavior. Freezing temperature distributions obtained from repeated experiments are shown for particle-free background and for 200 nm AgI particles (Fig. 3a). Background measurements were conducted by using particle-free nitrogen gas flow directed toward the supercooled droplet under otherwise identical conditions. In the absence of particles, freezing occurs over a relatively broad temperature range from -34.4 to -25.4 ℃ ($T_{50} = -28.8$℃; n=21), reflecting stochastic background freezing of pure-water droplets. The freezing temperature distribution of particle-free background is approximately unimodal and symmetric, indicating stable and reproducible baseline behavior. In contrast, freezing induced by 200 nm AgI particles is sharply shifted to higher temperatures and exhibits a much narrower and more concentrated spread (-13.9 to -11.8 ℃, $T_{50} = -12.6$℃; n=31), consistent with efficient and repeatable impact-initiated contact freezing. The upper bound of the background freezing distribution (-25.4 ℃) represents a conservative lower temperature limit for reliable C-ICE measurements. Above this temperature, freezing can be confidently attributed to particle-induced processes. Below this temperature, overlap with stochastic background freezing makes attribution increasingly uncertain.

https://doi.org/10.5194/egusphere-2026-3946
Preprint. Discussion started: 28 July 2026

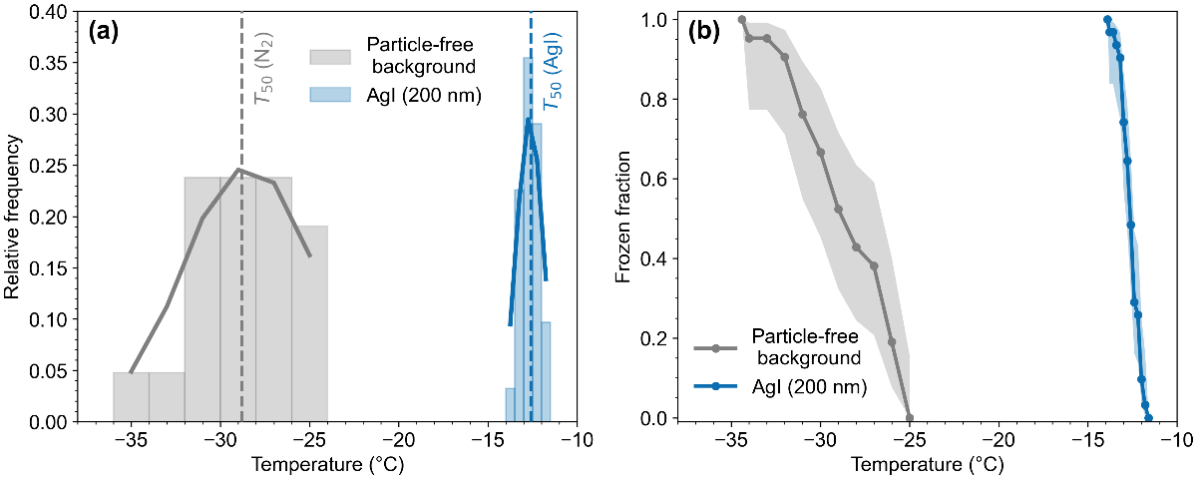

Figure 3: Freezing temperature distributions and frozen fraction for impact-initiated contact freezing in the C-ICE system. (a) Distributions of freezing temperatures obtained from repeated experiments conducted under identical conditions for the particle-free background (i.e., no aerosol particles present; grey; n = 21) and for 200 nm AgI particles (blue; n = 31). Histograms are shown as relative frequencies, such that the sum of bin heights equals unity for each dataset. The solid curves represent Gaussian-smoothed normalized histograms. Different bin widths are used to reflect the distinct temperature ranges and data densities of the two datasets (2.0 °C for particle-free background and 0.5 °C for AgI). Vertical dashed lines indicate the median freezing temperature (T_{50}) for each condition. (b) Frozen fraction as a function of temperature for the particle-free background and 200 nm AgI particles. Shaded regions represent the 95% confidence intervals calculated using the Wilson score method.

The corresponding frozen fraction curves shown in Fig. 3b further highlight the clear separation between background freezing and particle-induced contact freezing. The background frozen fraction increases gradually with decreasing temperature and reaches unity only at substantially lower temperatures, whereas the AgI frozen fraction transitions sharply over a narrow temperature interval at much higher temperatures. The narrow confidence intervals derived using the Wilson score method demonstrate that the observed differences are statistically robust. These results confirm that background freezing in C-ICE is both weak and well characterized, providing a reliable reference for quantifying particle-induced contact freezing. Freezing observed at higher temperatures is therefore attributable to aerosol-droplet interactions.

Beyond freezing statistics, controlled aerosol conditioning is essential for meaningful interpretation of impact-initiated contact freezing measurements. Figure 4 presents simulations of the thermodynamic evolution of water vapor within the dehumidifier section of the C-ICE system. This cylindrical dehumidifier simultaneously cools and dehumidifies the particle-laden airstream as it passes through the 1.0 m long cooled section. Under representative operating conditions (25 °C inlet temperature, 10% initial RH, and 1.5 L min^{-1} flow rate), the gas temperature decreases smoothly toward the chiller setpoint (-15 °C), crossing 0 °C within 0.15 m of the inlet. As temperature declines, the saturation vapor pressure (P_{sat}) correspondingly decreases while absolute water vapor content (actual water vapor pressure, P_v) remains nearly constant, leading to a continuous increase in RH with respect to both liquid water (RH_w) and ice (RH_i). Ice saturation (RH_i=1) is reached at 0.23 m of the inlet, beyond which excess water vapor is removed by deposition onto the cooled inner wall, resulting in effective dehumidification of the airstream. At the outlet, the particle-laden airflow reaches a temperature closely matched to the cold-stage droplet, minimizing unintended

https://doi.org/10.5194/egusphere-2026-3946
Preprint. Discussion started: 28 July 2026

condensation or frost formation in the collision region. This controlled thermodynamic state ensures that breath figure formation arises from localized latent heat release during freezing rather than from background humidity fluctuations.

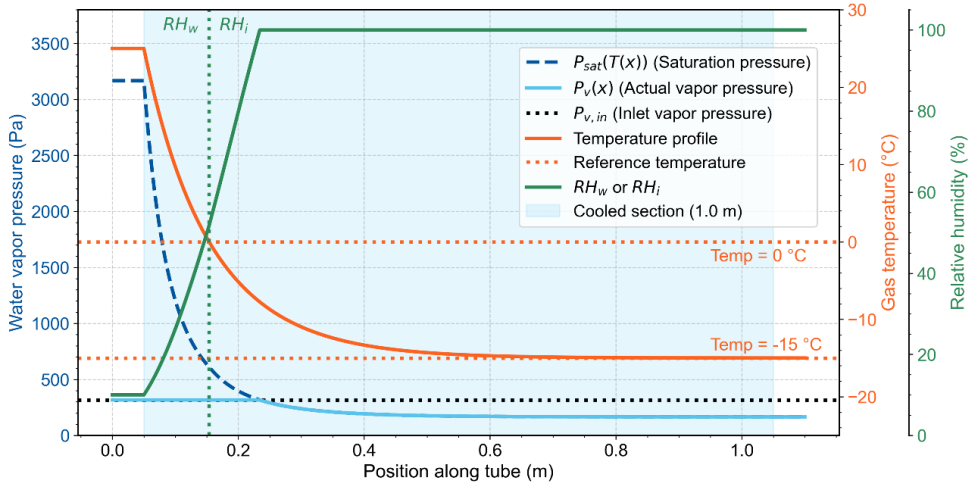

Figure 4: Simulated evolution of the thermodynamic state of water vapor in the dehumidifier section of the C-ICE system. Shown are the axial profiles of water vapor saturation pressure (P_{sat}; dashed blue line), actual water vapor pressure (P_v; solid light blue line), inlet water vapor pressure ($P_{v,in}$; dotted blue line), gas temperature (solid orange line), and relative humidity (RH; with respect to liquid water, RH_w, and with respect to ice, RH_i; solid green lines) along the dehumidifier tube. The shaded light blue region indicates the cooled section (length = 1.0 m), where the particle-laden airflow passes through the inner tube of a concentric double-tube dehumidifier, while temperature control is provided by an ethanol-based coolant circulating in the outer jacket. The simulation is performed for an inlet airstream at room temperature (25 °C) with an initial RH of 10% and a flow rate of 1.5 L min^{-1}. The chiller is set to a working temperature of -15 °C. Reference temperatures are indicated by dotted orange lines.

The robustness of the dehumidifier performance across a wide range of operating conditions is further demonstrated in Fig. S3, which shows simulated profiles of gas temperature, flow velocity, and Reynolds number (R_e) for flow rates ranging from 120 to 2000 cm^3 min^{-1}. In all cases, the flow remains well within the laminar regime throughout the cooled section ($R_e \ll 2300$). At the same time, the gas temperature approaches the coolant setpoint within a relatively short axial distance, even at the highest flow rates. These results confirm that the dehumidifier provides stable laminar flow and sufficient cooling capacity across the full experimental range.

Taken together, the results presented in Figs. 3, 4, and S3 demonstrate stable and reproducible system performance. Background freezing is well constrained and clearly separated from particle-induced events, while aerosol conditioning ensures controlled thermodynamic and flow conditions prior to collision.

3.3 Experimental constraints on collision efficiency in C-ICE

Quantifying the collision efficiency (CE) between aerosol particles and the target droplet is essential for interpreting impact-initiated contact freezing measurements in the C-ICE system. The number of particles that physically collide with the droplet is governed by the particle-droplet collision efficiency, which depends on particle properties, flow conditions, and experimental

https://doi.org/10.5194/egusphere-2026-3946
Preprint. Discussion started: 28 July 2026

geometry. In this section, we combine a physically based collision model with experimental constraints to derive a system-specific CE for the C-ICE configuration.

Figure 5 shows the modeled CE as a function of particle diameter, separated into contributions from six physical mechanisms: Brownian motion, inertial impaction, interception, thermophoresis, diffusiophoresis, and electric forces. Consistent with classical particle-droplet collection theory, Brownian motion is expected to dominate at small particle sizes, whereas inertial impaction becomes increasingly important at larger sizes. The total CE is calculated as the sum of these individual mechanisms under the experimental conditions of a particle-laden airstream with a flow rate of 120 cm^3 min^{-1}, a droplet surface temperature of -15 °C, an air temperature of -14.9 °C, and a RH_i of 90%. Electric effects are parameterized using an empirical charging coefficient α_q, which characterizes particle charge effects. The value of α_q ranges from 0 (electrically neutral particles) to 7 (highly electrified environments such as thunderstorms); a representative value of $\alpha_q = 0.1$ is adopted here (Andronache et al., 2006). The modeled results show that at smaller diameters ($d_p < 0.2$ µm), Brownian motion dominates the collision process, resulting in increasing CE with decreasing particle size. At larger diameters, inertial impaction and interception become increasingly important, producing a rapid rise in CE toward unity. Thermophoresis and electric forces contribute weakly under the present conditions, while diffusiophoresis is several orders of magnitude smaller than other mechanisms and is not visually distinguishable on the scale of Fig. 5. The combined effect of these mechanisms produces a characteristic U-shaped CE-diameter relationship, with a minimum at submicron sizes (approximately 0.15 µm) and a sharp increase toward unity for supermicron particles. This feature corresponds to the well-known Greenfield gap, a regime in which particles are too large for efficient Brownian motion yet too small for inertial impaction to be effective (Greenfield, 1957; Ladino et al., 2011a). In this size range, neither diffusive nor inertial collection mechanisms dominate, and interception remains weak, leading to minimal particle-droplet collision probabilities.

Although this model captures the expected behavior qualitatively, the Greenfield gap regime corresponds to particle sizes for which the predicted CE is very low and therefore sensitive to uncertainties in flow geometry, particle trajectories, and weak or unresolved collection processes. Unfortunately, this size range is important for particle-droplet interactions in the atmosphere (Ladino Moreno et al., 2013). To better constrain the model, we therefore derive experimental lower-bound CE values from contact freezing measurements using monodisperse AgI particles of 200 and 800 nm diameter. To do so, we assume a single effective particle-droplet collision during a short temperature interval is sufficient to trigger a contact freezing event.

https://doi.org/10.5194/egusphere-2026-3946
Preprint. Discussion started: 28 July 2026

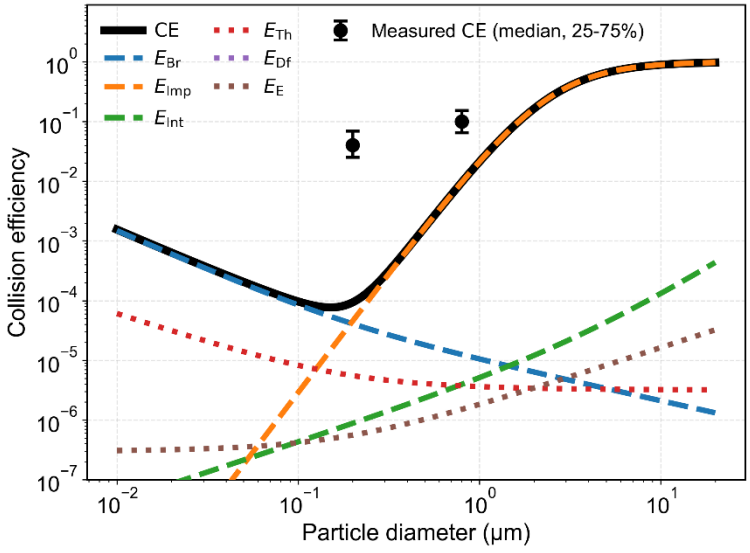

Figure 5: Modeled collision efficiency (CE) for aerosol-droplet collisions in the C-ICE configuration as a function of particle diameter. Individual contributions from Brownian motion (E_{Br}, dashed blue line), inertial impaction (E_{Imp}, dashed orange line), interception (E_{Int}, dashed green line), thermophoresis (E_{Th}, dotted red line), diffusiophoresis (E_{Df}, dotted purple line), and electric forces (E_{E}, dotted brown line) are shown together with their combined total collision efficiency (CE, solid black line). Under the present experimental conditions, the contribution from diffusiophoresis is several orders of magnitude smaller than the other mechanisms and is therefore not visually distinguishable at the scale of the figure. Black circles represent experimentally measured collision efficiencies of 200nm and 800nm AgI particles, shown as the median with interquartile range (25-75%).

In the experiments, the cold stage cools at a rate of 1 °C min^{-1}, corresponding to a time interval of $\Delta t = 6\ s$ for a temperature decrement of 0.1 °C. The aerosol flow rate (Q) is maintained at 120 cm^3 min^{-1}, and the particle number concentration ($N_{particle}$) downstream of the conditioning unit is continuously monitored using a CPC. For each experiment, particle concentrations are deliberately kept low to minimize the number of particles colliding with a single droplet and to allow robust estimation of collision efficiency from freezing statistics.

Under these conservative conditions, the experimentally inferred collision efficiency can be estimated as

$$\mathrm{CE}_{\mathrm{exp}} = \frac{1}{\Delta t \cdot Q \cdot N_{particle}} \tag{12}$$

This estimate represents a lower bound on the true collision efficiency, as it assumes that exactly one effective collision is required to trigger freezing within the considered time interval. Accordingly, $\mathrm{CE}_{\mathrm{exp}}$ is not an intrinsic property of the system but a conservative lower-bound estimate under the specified experimental conditions.

Using this approach, experimentally inferred median collision efficiencies of 0.04 for 200 nm AgI (0.03-0.07, 25-75%; mean=0.05; n=29) and 0.10 for 800 nm AgI (0.07-0.15, 25-75%; mean=0.11; n=32) are obtained (shown as black symbols in Figs. 5 and 6; Table S2). These values substantially exceed the corresponding pure model predictions (9.7×10^{-5} for 200 nm and 0.01 for 800 nm), indicating that the theoretical formulation underestimates collision probabilities under the specific thermodynamic conditions of C-ICE. Compared with previous studies, Nagare et al. (2015) inferred collision efficiencies of

https://doi.org/10.5194/egusphere-2026-3946
Preprint. Discussion started: 28 July 2026

0.13 for 200 nm AgI and 0.07 for 400 nm AgI using the CoLlision Ice Nucleation CHamber (CLINCH), in which ~80 μm droplets sediment through an aerosol-filled chamber. Although the magnitudes are broadly comparable, direct quantitative comparison is complicated by substantial differences in droplet size, flow geometry, particle-droplet relative velocity, and residence time between the two systems. In another laboratory experimental configuration, Ardon-Dryer et al. (2015) reported CE values ranging from 0.015 to 0.09 under high RH conditions (88±3%) using the Massachusetts Institute of Technology Collection Efficiency Chamber (MIT-CEC).

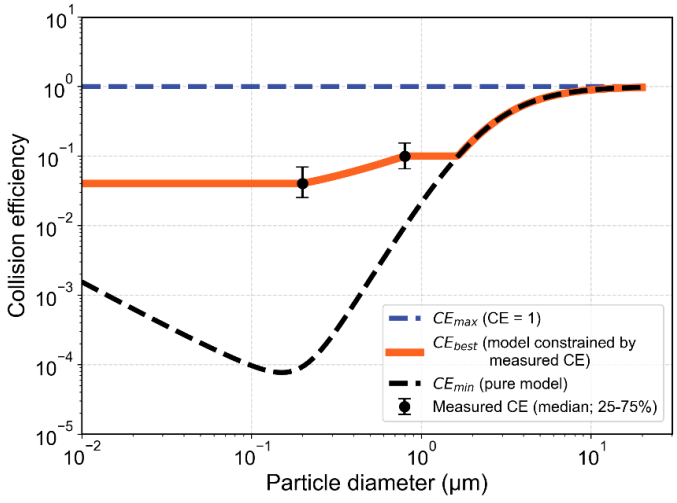

Figure 6: Experimentally constrained collision efficiency for the C-ICE system. The pure model prediction assuming only physically resolved collection mechanisms (CE_{min}, dashed black line), the upper bound assuming unit collision efficiency ($CE_{max} = 1$, dashed blue line), and the best-estimate collision efficiency (CE_{best}, solid orange line) constrained by experimental results for 200 nm and 800 nm AgI particles are shown as a function of particle diameter. Black circles indicate experimentally inferred collision efficiencies, shown as the median with interquartile range (25-75%).

To reconcile model predictions with experimental constraints, we construct and compare three CE scenarios in Fig. 6, including: (i) a model-based minimum (CE_{min}), defined as the theoretical model prediction without experimental adjustment; (ii) an idealized upper bound ($CE_{max} = 1$), assuming all particles collide with the droplet; and (iii) an observation-constrained best estimate (CE_{best}). The CE_{best} curve is constructed by imposing an empirical lower envelope based on the experimentally inferred median CE values at 200 nm and 800 nm (0.04 and 0.10, respectively), using linear interpolation between these sizes and constant extrapolation outside this range, while retaining the model prediction where it exceeds the empirical constraint. This formulation ensures that CE_{best} does not fall below experimentally supported values and avoids unphysical suppression of collision efficiency at larger particle sizes. As shown in Figs. 6 and S4, the experimentally inferred CE_{best} fall between CE_{min} and CE_{max}. The constrained efficiency increases from 0.04 at 200 nm to 0.10 at 800 nm, consistent with the increasing contribution of inertial impaction and interception at larger particle sizes. Importantly, CE_{best} provides a smooth and physically consistent transition across the particle size range, reconciling model behavior with observed freezing responses. The resulting CE_{best} is subsequently used to convert measured aerosol number concentrations and size distributions into effective particle collision rates onto the droplet, enabling a quantitative interpretation of frozen fraction measurements. This conversion is

https://doi.org/10.5194/egusphere-2026-3946
Preprint. Discussion started: 28 July 2026

particularly important for polydisperse aerosols, for which particle-droplet collision frequencies depend strongly on particle size.

3.4 Frozen fraction of AgI aerosols

The frozen fraction behavior of AgI aerosols measured in C-ICE as a function of particle size is summarized in Fig. 7. Figure 7a shows the frozen fraction as a function of temperature for monodisperse AgI particles (200 and 800 nm) and for the polydisperse AgI aerosol. All three cases exhibit sharp frozen fraction curves over relatively narrow temperature intervals, confirming the high ice nucleation efficiency of AgI by impact-initiated contact freezing.

Clear differences are observed among the three particle populations. For monodisperse AgI, the 800 nm particles froze at slightly higher temperatures (-12.7 to -11.5 ℃, $T_{50} = -12.0$℃; n=34) than the 200 nm particles (-13.9 to -11.8 ℃, $T_{50} = -12.6$℃; n=31) (Table S1). The polydisperse aerosol exhibits freezing at still higher temperatures and over a broader interval (-11.1 to -9.2 ℃, $T_{50} = -10.1$℃; n=50), reflecting contributions from coarse-mode particles. In addition, monodisperse particles show steeper frozen fraction slopes than the polydisperse case, indicating a more narrowly defined freezing threshold. These differences persist under identical thermodynamic and flow conditions, demonstrating that they cannot be attributed to background freezing or experimental instability. Instead, the systematic shift in frozen fraction curves with particle size highlights the sensitivity of impact-initiated contact freezing to particle properties and particle-droplet interaction dynamics. The underlying mechanism is not explicitly resolved by the present experiments. However, larger particles may promote freezing through a combination of increased contact area, greater collision momentum, and a higher probability of containing active nucleation sites, all of which have been proposed as factors contributing to enhanced contact freezing efficiency (Ladino Moreno et al., 2013). While the present dataset is limited to two monodisperse sizes and one polydisperse population, the results provide direct evidence for a potential particle-size dependence of contact freezing behavior, consistent with previous observations for mineral dust particles (Hoffmann et al., 2013a). Importantly, these results demonstrate that C-ICE enables size-resolved constraints on contact freezing under controlled collision conditions.

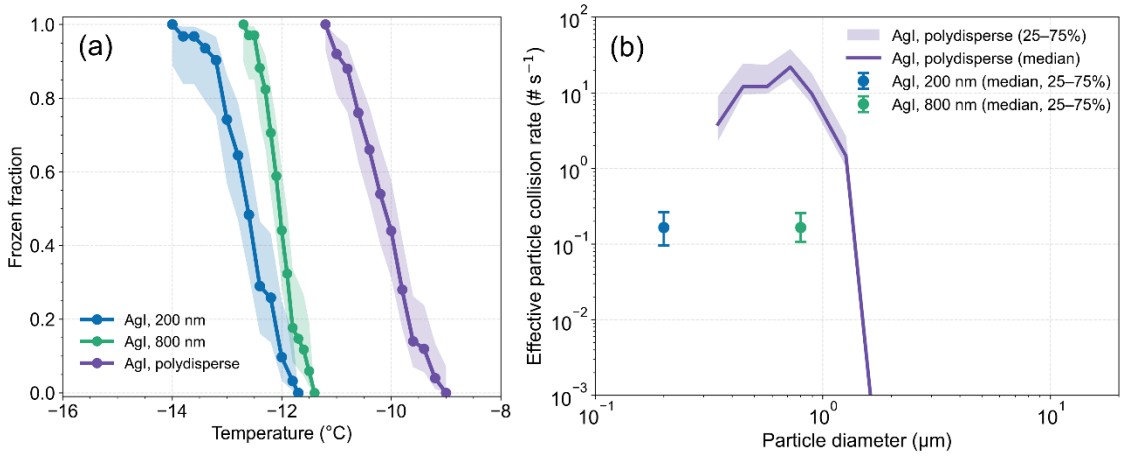

https://doi.org/10.5194/egusphere-2026-3946
Preprint. Discussion started: 28 July 2026

Figure 7: Frozen fraction and effective particle collision rate for AgI aerosols under controlled collision conditions in the C-ICE system. (a) Frozen fraction as a function of temperature for monodisperse AgI particles with diameters of 200 nm and 800 nm, and for the polydisperse AgI aerosol. Shaded regions represent the 95% confidence intervals calculated using the Wilson score method. (b) Effective particle collision rate onto the target droplet for the same experiments shown in panel (a), expressed as the number of particles colliding with the droplet per second. The collision rate is calculated by combining measured aerosol number concentrations (from CPC and OPC measurements) with the experimentally constrained collision efficiency (CE_{best}) and the aerosol flow rate (120 cm^3 min^{-1}). Following the discussion in Sect. 3.3, the effective particle collision rate shown here should be regarded as a conservative lower bound. Results for the polydisperse AgI aerosol are summarized as the median (solid purple line) with the interquartile range (25-75%; shaded). For size-selected aerosols (200 nm and 800 nm), the median values and interquartile ranges are shown as markers with error bars.

To help interpret the differences among the frozen fraction results, Fig. 7b presents the effective particle collision rate onto the target droplet, expressed as the number of particles colliding with the droplet per second. Rates are calculated from measured aerosol number concentrations (CPC and OPC) combined with the experimentally constrained collision efficiency CE_{best} (Sect. 3.3) and the known aerosol flow rate. For the monodisperse cases, particle number concentrations are derived from DMA-selected aerosols, which represent a narrow size bin. In contrast, the polydisperse case is characterized using OPC measurements with size bins spanning several hundred nanometers, representing a broader size range. As a result, the comparison between monodisperse and polydisperse particle rates is not strictly equivalent and should be interpreted with this difference in mind. Despite differences in aerosol number concentration between experiments, the median effective particle collision rate is identical for the two monodisperse cases, with values of 0.17 s^{-1} for both 200 nm and 800 nm AgI. The corresponding mean rates are 0.20 s^{-1} and 0.29 s^{-1}, respectively (Table S3), providing a robust basis for comparison under comparable effective collision conditions. In contrast, the polydisperse aerosol produces substantially higher collision rates over much of the size range. Submicron particles alone contribute on the order of ~10 collisions per second, far exceeding the monodisperse cases, and additional contributions arise from coarse-mode particles (~1 collision per second). The higher effective collision rate increases the probability that the droplet encounters active AgI particles within a given temperature interval, which likely contributes to the higher freezing temperatures observed for the polydisperse aerosol. At the same time, the broader freezing temperature range and more gradual frozen fraction curve are more directly attributable to the broad particle size distribution, because particles of different sizes can differ in collision efficiency, contact area, momentum, and probability of containing active nucleation sites. Particle number concentrations and size distributions are shown in Figs. S5 and S6 and Table S4. Thus, the frozen fraction curve reflects both particle ice-nucleating properties and the size-dependent collision rate, with the curve width influenced by the spread of particle sizes and the curve position mainly influenced by the frequency of effective particle-droplet encounters and associated freezing responses.

It is important to emphasize that the effective particle collision rates shown in Fig. 7b represent conservative lower-bound estimates, because CE_{best} is constructed as a lower envelope constrained by experimental measurements at 200 nm and 800 nm (Sect. 3.3). In addition, the calculation assumes that a single effective collision within a given temperature interval is sufficient to trigger freezing, and does not account for multiple ineffective collisions or partial contacts. Consequently, the true particle-droplet collision rates are likely higher than those reported here.

https://doi.org/10.5194/egusphere-2026-3946
Preprint. Discussion started: 28 July 2026

The frozen fraction results for AgI in this study are broadly consistent with previous contact freezing measurements. Submicron AgI particles (200 nm) are observed to initiate freezing at temperatures near -12 °C, in agreement with earlier studies from the CLINCH chamber (Nagare et al., 2016). However, the frozen fraction curves obtained with C-ICE exhibit a much sharper transition, with freezing occurring within a narrow temperature interval of ~2 °C. In contrast, chamber-based studies often report freezing over a substantially broader temperature range, extending to much lower temperatures (~-35 °C). Moreover, Marcolli et al. (2016) summarized numerous studies showing that AgI exhibits strong mode dependence, with reported contact freezing temperatures varying widely with particle size (surface area), droplet size, and experimental configuration. For example, Schiffman et al. (2025) recently reported surface-initiated contact freezing for large AgI particles (~380 μm) with a mean freezing temperature of -5.4 ± 1.1 °C, substantially warmer than the submicron aerosol results reported here. Earlier experimental studies similarly reported median freezing spanning from approximately -5 °C to -25 °C, depending on droplet size, aerosol loading, and flow conditions (Gokhale and Goold, 1968; Sax and Goldsmith, 1972; Langer et al., 1978; DeMott, 1995; Nagare et al., 2016).

These differences do not indicate inconsistency among studies, but instead reflect fundamental differences in particle size, collision regime, droplet size, and thermodynamic control. Chamber experiments inherently convolve nucleation efficiency with collision statistics governed by turbulence, residence time, and stochastic droplet-particle encounters. Surface-initiated studies emphasize interfacial attachment with minimal inertia. In contrast, C-ICE imposes directed and repeatable particle-droplet impacts under well-defined conditions. As a result, the frozen fraction curves more directly reflect the temperature-dependent nucleation response following effective collision.

In conclusion, C-ICE enables size-resolved quantification of impact-initiated contact freezing under controlled conditions. The measurements produce frozen fraction curves with sharper transitions than those typically reported in chamber-based studies, reflecting the well-defined collision conditions. While AgI serves as a benchmark INP, the method is readily extendable to other aerosol types and size ranges. This provides a quantitative basis for constraining contact freezing parameterizations and for isolating the role of collision dynamics in aerosol-cloud interactions.

4 Conclusions

This study establishes the Cold-stage system for Impact-initiated Contact freezing Experiments (C-ICE) as a quantitative experimental system for controlled, repeatable, and size-resolved investigations of impact-initiated contact freezing. By combining a fixed supercooled droplet with a precisely conditioned aerosol jet, C-ICE enforces well-defined particle-droplet collisions while independently characterizing aerosol size, number concentration, and thermodynamic state. Freezing onset is identified at the single-droplet level using complementary optical criteria based on breath figure formation and grayscale analysis. This allows collision-triggered freezing to be distinguished from complete freezing and from procedural blank events. Background measurements show that spontaneous freezing is weak and reproducible and define a conservative operating window (T > -25.4 °C) in which particle-induced freezing is clearly separated from droplet-only freezing. Application to AgI

https://doi.org/10.5194/egusphere-2026-3946
Preprint. Discussion started: 28 July 2026

aerosols reveals sharp frozen fraction transitions over narrow temperature intervals, with systematic shifts toward higher temperatures for larger particle sizes and for polydisperse populations. These results indicate a potential size effect in freezing behavior, although additional measurements across a wider size range are needed to establish a quantitative relationship. By integrating a physically based collision model with experimentally inferred lower-bound collision efficiencies, we derive a system-specific and experimentally constrained collision efficiency (CE_{best}) for C-ICE. This provides a physically interpretable link between measured aerosol concentrations and the effective particle collision rate onto the droplet, allowing frozen fraction measurements to be interpreted under collision-controlled conditions.

These results have broader implications for contact freezing and aerosol-cloud interactions. The steep frozen fraction curves observed here highlight the importance of explicitly controlling and quantifying particle-droplet collisions when interpreting contact freezing data. More generally, frozen fraction measurements reflect not only intrinsic ice nucleation activity, but also particle size, collision probability, and interaction dynamics. The ability to impose repeatable and size-resolved collision conditions provides a pathway for constraining contact freezing parameterizations with reduced ambiguity. Extending C-ICE to other INP types, droplet sizes, and flow conditions will enable systematic investigation across particle types and scales, providing physically grounded constraints for representing contact freezing in cloud microphysical models.

Appendix A

Table A1. List of symbols

AgI	Silver iodide
C_c	Cunningham slip correction factor
CCD	Charge-coupled device
CE	Collision efficiency
CE_{best}	Experimentally constrained best-estimate collision efficiency
CE_{exp}	Experimentally inferred collision efficiency
CE_{max}	Collision efficiency assuming unit collection efficiency
CE_{min}	Collision efficiency predicted by the physical model
C-ICE	Cold-stage system for Impact-initiated Contact freezing Experiments
CPC	Condensation particle counter
D_d	Droplet diameter
D_{diff}	Particle diffusion coefficient
d_p	Particle diameter
DMA	Differential mobility analyzer
EDB	Electrodynamic balance

https://doi.org/10.5194/egusphere-2026-3946
Preprint. Discussion started: 28 July 2026

E_{Br}	Collision efficiency due to Brownian motion
E_{Df}	Collision efficiency due to diffusiophoresis
E_E	Collision efficiency due to electric forces
E_{Imp}	Collision efficiency due to inertial impaction
E_{Int}	Collision efficiency due to interception
E_{Th}	Collision efficiency due to thermophoresis
$f_{ice}(T)$	Frozen fraction at temperature T
INPs	Ice nucleating particles
K	Coulomb constant
k_{B}	Boltzmann constant
λ	Mean free path of air molecules
μ	Air viscosity
$N_f(T)$	Cumulative number of droplets frozen at temperatures $\geq T$
$N_{particle}$	Particle number concentration
N_{tot}	Total number of droplets
OPC	Optical particle counter
p_a^0	Water vapor pressure at temperature T_a
p_s^0	Water vapor pressure at temperature T_s
Pe	Peclet number
P_r	Prandtl number of air
P_{sat}	Saturation vapor pressure
P_v	Actual water vapor pressure
$P_{v,in}$	Inlet water vapor pressure
R_e	Reynolds number
RH	Ambient relative humidity
RH_i	Relative humidity with respect to ice
RH_w	Relative humidity with respect to liquid water
ρ_{p}	Particle density
S_{c_w}	Schmidt number of water vapor in air
Stk	Stokes number
T_{50}	Median freezing temperature

https://doi.org/10.5194/egusphere-2026-3946
Preprint. Discussion started: 28 July 2026

T_a	Absolute temperature of air
T_s	Absolute temperature of droplet surface
UHPLC	Ultra-high-performance liquid chromatography
σ	Viscosity ratio of water to air
Q	Aerosol flow rate
U	Particle approach velocity at the moment of particle-droplet collision

Data availability

All data supporting the findings of this study are provided in the article and the Supplement. The datasets used to generate the figures are available from the Texas Data Repository at https://doi.org/10.18738/T8/4LM3BB. Additional information is available from the corresponding author upon reasonable request.

Supplement link

The Supplement related to this article is available online

Author contributions

J.C. and S.B. conceived the study. J.C. developed the C-ICE methodology, conducted the experiments, performed data analysis and visualization, and prepared the manuscript. S.B., U.R., K.M., R.D., and M.T. contributed to data interpretation and manuscript revision. All authors discussed the results and contributed to the writing of this paper.

Competing interests

The authors declare no conflicts of interest relevant to this study.

Disclaimer

Copernicus Publications remains neutral with regard to jurisdictional claims made in the text, published maps, institutional affiliations, or any other geographical representation in this paper. While Copernicus Publications makes every effort to include appropriate place names, the final responsibility lies with the authors. Views expressed in the text are those of the authors and do not necessarily reflect the views of the publisher.

https://doi.org/10.5194/egusphere-2026-3946
Preprint. Discussion started: 28 July 2026

Sandia National Laboratories is a multimission laboratory managed and operated by National Technology & Engineering Solutions of Sandia, LLC, a wholly owned subsidiary of Honeywell International Inc., for the U.S. Department of Energy's National Nuclear Security Administration under contract DE-NA0003525. This paper describes objective technical results and analysis. Any subjective views or opinions that might be expressed in the paper do not necessarily represent the views of the U.S. Department of Energy or the United States Government.

Acknowledgements

The authors thank Bo Chen, Seth A. Thompson, Roya Safa, and Taylor A. Peña at Texas A&M University for helpful discussions and assistance related to this work.

Financial support

This research was supported by National Science Foundation Grant AGS-2346198.

References

Agresti, A., and Coull, B. A.: Approximate is Better than "Exact" for Interval Estimation of Binomial Proportions, The American Statistician, 52, 119-126, 10.1080/00031305.1998.10480550, 1998.

Alsante, A. N., Thornton, D. C. O., and Brooks, S. D.: Effect of Aggregation and Molecular Size on the Ice Nucleation Efficiency of Proteins, Environ Sci Technol, 58, 4594-4605, 10.1021/acs.est.3c06835, 2024.

Andronache, C., Grönholm, T., Laakso, L., Phillips, V., and Venäläinen, A.: Scavenging of ultrafine particles by rainfall at a boreal site:: observations and model estimations, Atmospheric Chemistry and Physics, 6, 4739-4754, DOI 10.5194/acp-6-4739-2006, 2006.

Ardon-Dryer, K., Huang, Y. W., and Cziczo, D. J.: Laboratory studies of collection efficiency of sub-micrometer aerosol particles by cloud droplets on a single-droplet basis, Atmospheric Chemistry and Physics, 15, 9159-9171, 10.5194/acp-15-9159-2015, 2015.

Baker, T. J.: LXV. Breath Figures, The London, Edinburgh, and Dublin Philosophical Magazine and Journal of Science, 44, 752-765, 10.1080/14786441108634040, 1922.

Beysens, D., and Knobler, C. M.: Growth of Breath Figures, Physical Review Letters, 57, 1433-1436, 10.1103/PhysRevLett.57.1433, 1986.

Biswas, S., Paul, D., Mondal, K., and Kaiser, R. I.: Simulating atmospheric freezing of single aqueous droplets to ice in a cryogenically cooled ultrasonic levitator, Proc Natl Acad Sci U S A, 122, e2425543122, 10.1073/pnas.2425543122, 2025.

Bouillant, A., Snoeijer, J. H., and Andreotti, B.: Collective effects in breath figures, Physical Review Fluids, 10, 10.1103/PhysRevFluids.10.053605, 2025.

Brooks, S. D., Suter, K., and Olivarez, L.: Effects of Chemical Aging on the Ice Nucleation Activity of Soot and Polycyclic Aromatic Hydrocarbon Aerosols, The Journal of Physical Chemistry A, 118, 10036-10047, 10.1021/jp508809y, 2014.

Budke, C., and Koop, T.: BINARY: an optical freezing array for assessing temperature and time dependence of heterogeneous ice nucleation, Atmospheric Measurement Techniques, 8, 689-703, 10.5194/amt-8-689-2015, 2015.

Burrows, S. M., McCluskey, C. S., Cornwell, G., Steinke, I., Zhang, K., Zhao, B., Zawadowicz, M., Raman, A., Kulkarni, G., China, S., Zelenyuk, A., and DeMott, P. J.: Ice-Nucleating Particles That Impact Clouds and Climate: Observational and Modeling Research Needs, Reviews of Geophysics, 60, 10.1029/2021rg000745, 2022.

https://doi.org/10.5194/egusphere-2026-3946
Preprint. Discussion started: 28 July 2026

Calvert, S.: Particle control by scrubbing, in: Handbook of Air Pollution Technology, edited by: Calvert, S., and Englund, H. M., Wiley, New York, 215-248, 1984.
Chen, J., Xu, J., Wu, Z., Meng, X., Yu, Y., Ginoux, P., DeMott, P. J., Xu, R., Zhai, L., Yan, Y., Zhao, C., Li, S.-M., Zhu, T., and Hu, M.: Decreased dust particles amplify the cloud cooling effect by regulating cloud ice formation over the Tibetan Plateau, Science Advances, 10, eado0885, 10.1126/sciadv.ado0885, 2024.
Chu, F., Li, S., Zhao, C., Feng, Y., Lin, Y., Wu, X., Yan, X., and Miljkovic, N.: Interfacial ice sprouting during salty water droplet freezing, Nat Commun, 15, 2249, 10.1038/s41467-024-46518-y, 2024.
Collier, K. N., and Brooks, S. D.: Role of Organic Hydrocarbons in Atmospheric Ice Formation via Contact Freezing, The Journal of Physical Chemistry A, 120, 10169-10180, 10.1021/acs.jpca.6b11890, 2016.
Cooper, W. A.: A Possible Mechanism for Contact Nucleation, Journal of Atmospheric Sciences, 31, 1832-1837, 10.1175/1520-0469(1974)031<1832:APMFCN>2.0.CO;2, 1974.
Creamean, J. M., Hume, C. C., Vazquez, M., and Theisen, A.: Long-term measurements of ice nucleating particles at Atmospheric Radiation Measurement (ARM) sites worldwide, Earth System Science Data, 17, 6943-6963, 10.5194/essd-17-6943-2025, 2025.
Davenport, H. M., and Peters, L. K.: Field Studies of Atmospheric Particulate Concentration Changes during Precipitation, Atmospheric Environment, 12, 997-1008, Doi 10.1016/0004-6981(78)90344-X, 1978.
DeMott, P. J.: Quantitative descriptions of ice formation mechanisms of silver iodide-type aerosols, Atmos. Res., 38, 63-99, 10.1016/0169-8095(94)00088-U, 1995.
DeMott, P. J., Mirrielees, J. A., Petters, S. S., Cziczo, D. J., Petters, M. D., Bingemer, H. G., Hill, T. C. J., Froyd, K., Garimella, S., Hallar, A. G., Levin, E. J. T., McCubbin, I. B., Perring, A. E., Rapp, C. N., Schiebel, T., Schrod, J., Suski, K. J., Weber, D., Wolf, M. J., Zawadowicz, M., Zenker, J., Möhler, O., and Brooks, S. D.: Field intercomparison of ice nucleation measurements: the Fifth International Workshop on Ice Nucleation Phase 3 (FIN-03), Atmospheric Measurement Techniques, 18, 639-672, 10.5194/amt-18-639-2025, 2025.
Diehl, K., Matthias-Maser, S., Jaenicke, R., and Mitra, S. K.: The ice nucleating ability of pollen: Part II. Laboratory studies in immersion and contact freezing modes, Atmos. Res., 61, 125-133, Pii S0169-8095(01)00132-6
Doi 10.1016/S0169-8095(01)00132-6, 2002.
Durant, A. J., and Shaw, R. A.: Evaporation freezing by contact nucleation inside-out, Geophys. Res. Lett., 32, 10.1029/2005gl024175, 2005.
Fletcher, N. H.: Active Sites and Ice Crystal Nucleation, Journal of Atmospheric Sciences, 26, 1266-1271, 10.1175/1520-0469(1969)026<1266:ASAICN>2.0.CO;2, 1969.
Fornea, A. P., Brooks, S. D., Dooley, J. B., and Saha, A.: Heterogeneous freezing of ice on atmospheric aerosols containing ash, soot, and soil, J. Geophys. Res.-Atmos., 114, 10.1029/2009jd011958, 2009.
Gokhale, N. R., and Goold, J.: Droplet Freezing by Surface Nucleation, Journal of Applied Meteorology (1962-1982), 7, 870-874, 1968.
Gong, X., Wex, H., van Pinxteren, M., Triesch, N., Fomba, K. W., Lubitz, J., Stolle, C., Robinson, T. B., Müller, T., Herrmann, H., and Stratmann, F.: Characterization of aerosol particles at Cabo Verde close to sea level and at the cloud level – Part 2: Ice-nucleating particles in air, cloud and seawater, Atmos. Chem. Phys., 20, 1451-1468, 10.5194/acp-20-1451-2020, 2020.
Greenfield, S. M.: Rain Scavenging of Radioactive Particulate Matter from the Atmosphere, Journal of Meteorology, 14, 115-125, 10.1175/1520-0469(1957)014<0115:Rsorpm>2.0.Co;2, 1957.
Harrison, A. D., Whale, T. F., Rutledge, R., Lamb, S., Tarn, M. D., Porter, G. C. E., Adams, M. P., McQuaid, J. B., Morris, G. J., and Murray, B. J.: An instrument for quantifying heterogeneous ice nucleation in multiwell plates using infrared emissions to detect freezing, Atmospheric Measurement Techniques, 11, 5629-5641, 10.5194/amt-11-5629-2018, 2018.
Hazra, A., Mallick, C., Mohan, G. M., Vani, K. G., Kumar, V. A., Chowdhury, R., Chaudhari, H. S., Das, S. K., Konwar, M., Pokhrel, S., Deshpande, S., Ghude, S. D., Pandithurai, G., and Pawar, S. D.: Understanding the impact of ice nucleation on lightning and rainfall: A case study, Atmos. Res., 278, 106350, 10.1016/j.atmosres.2022.106350, 2022.
Hoffmann, N., Duft, D., Kiselev, A., and Leisner, T.: Contact freezing efficiency of mineral dust aerosols studied in an electrodynamic balance: quantitative size and temperature dependence for illite particles, Faraday Discussions, 165, 383-390, 10.1039/C3FD00033H, 2013a.
Hoffmann, N., Kiselev, A., Rzesanke, D., Duft, D., and Leisner, T.: Experimental quantification of contact freezing in an electrodynamic balance, Atmospheric Measurement Techniques, 6, 2373-2382, 10.5194/amt-6-2373-2013, 2013b.

https://doi.org/10.5194/egusphere-2026-3946
Preprint. Discussion started: 28 July 2026

Hoose, C., and Mohler, O.: Heterogeneous ice nucleation on atmospheric aerosols: a review of results from laboratory experiments, Atmospheric Chemistry and Physics, 12, 9817-9854, 10.5194/acp-12-9817-2012, 2012.
Jung, C. H., and Lee, K. W.: Filtration of Fine Particles by Multiple Liquid Droplet and Gas Bubble Systems, Aerosol Science and Technology, 29, 389-401, 10.1080/02786829808965578, 1998.
Kalita, A., Mrozek-McCourt, M., Kaldawi, T. F., Willmott, P. R., Loh, N. D., Marte, S., Sierra, R. G., Laksmono, H., Koglin, J. E., Hayes, M. J., Paul, R. H., Guillet, S. A. H., Aquila, A. L., Liang, M., Boutet, S., and Stan, C. A.: Microstructure and crystal order during freezing of supercooled water drops, Nature, 620, 557-561, 10.1038/s41586-023-06283-2, 2023.
Kanji, Z. A., Ladino, L., Wex, H., Boose, Y., Burkert-Kohn, M., Cziczo, D., and Krämer, M.: Ice Formation and Evolution in Clouds and Precipitation: Measurement and Modeling Challenges. Chapter 1: Overview of Ice Nucleating Particles, Meteorological Monographs, 58, 1-25, 10.1175/AMSMONOGRAPHS-D-0006.1, 2017.
Kiselev, A., Bachmann, F., Pedevilla, P., Cox, S. J., Michaelides, A., Gerthsen, D., and Leisner, T.: Active sites in heterogeneous ice nucleation—the example of K-rich feldspars, Science, 355, 367-371, 10.1126/science.aai8034, 2017.
Knopf, D. A., and Koop, T.: Heterogeneous nucleation of ice on surrogates of mineral dust, Journal of Geophysical Research: Atmospheres, 111, 10.1029/2005jd006894, 2006.
Knopf, D. A., and Alpert, P. A.: Atmospheric ice nucleation, Nature Reviews Physics, 5, 203-217, 10.1038/s42254-023-00570-7, 2023.
Ladino, L., Stetzer, O., Hattendorf, B., Günther, D., Croft, B., and Lohmann, U.: Experimental Study of Collection Efficiencies between Submicron Aerosols and Cloud Droplets, Journal of the Atmospheric Sciences, 68, 1853-1864, 10.1175/JAS-D-11-012.1, 2011a.
Ladino, L., Stetzer, O., Lüönd, F., Welti, A., and Lohmann, U.: Contact freezing experiments of kaolinite particles with cloud droplets, Journal of Geophysical Research: Atmospheres, 116, 10.1029/2011JD015727, 2011b.
Ladino Moreno, L. A., Stetzer, O., and Lohmann, U.: Contact freezing: a review of experimental studies, Atmospheric Chemistry and Physics, 13, 9745-9769, 10.5194/acp-13-9745-2013, 2013.
Langer, G., Cooper, G., Nagamoto, C. T., and Rosinski, J.: Ice Nucleation Mechanisms of Submicron Monodispersed Silver Iodide, 1,5-Dihydroxynaphthalene and Phloroglucinol Aerosol Particles, Journal of Applied Meteorology and Climatology, 17, 1039-1048, 10.1175/1520-0450(1978)017<1039:INMOSM>2.0.CO;2, 1978.
Lohmann, U., Lüönd, F., and Mahrt, F.: An Introduction to Clouds: From the Microscale to Climate, Cambridge University Press, Cambridge, 2016.
Marcolli, C., Nagare, B., Welti, A., and Lohmann, U.: Ice nucleation efficiency of AgI: review and new insights, Atmospheric Chemistry and Physics, 16, 8915-8937, 10.5194/acp-16-8915-2016, 2016.
Matthews, B. H., Alsante, A. N., and Brooks, S. D.: Pollen Emissions of Subpollen Particles and Ice Nucleating Particles, ACS Earth Space Chem, 7, 1207-1218, 10.1021/acsearthspacechem.3c00014, 2023.
McCluskey, C. S., Hill, T. C. J., Humphries, R. S., Rauker, A. M., Moreau, S., Strutton, P. G., Chambers, S. D., Williams, A. G., McRobert, I., Ward, J., Keywood, M. D., Harnwell, J., Ponsonby, W., Loh, Z. M., Krummel, P. B., Protat, A., Kreidenweis, S. M., and DeMott, P. J.: Observations of Ice Nucleating Particles Over Southern Ocean Waters, Geophys. Res. Lett., 45, 11,989-911,997, 10.1029/2018GL079981, 2018.
Murray, B. J., O'Sullivan, D., Atkinson, J. D., and Webb, M. E.: Ice nucleation by particles immersed in supercooled cloud droplets, Chem Soc Rev, 41, 6519-6554, 10.1039/c2cs35200a, 2012.
Nagare, B., Marcolli, C., Stetzer, O., and Lohmann, U.: Comparison of measured and calculated collision efficiencies at low temperatures, Atmospheric Chemistry and Physics, 15, 13759-13776, 10.5194/acp-15-13759-2015, 2015.
Nagare, B., Marcolli, C., Welti, A., Stetzer, O., and Lohmann, U.: Comparing contact and immersion freezing from continuous flow diffusion chambers, Atmospheric Chemistry and Physics, 16, 8899-8914, 10.5194/acp-16-8899-2016, 2016.
Niedermeier, D., Shaw, R. A., Hartmann, S., Wex, H., Clauss, T., Voigtländer, J., and Stratmann, F.: Heterogeneous ice nucleation: exploring the transition from stochastic to singular freezing behavior, Atmospheric Chemistry and Physics, 11, 8767-8775, 10.5194/acp-11-8767-2011, 2011.
Park, S. H., Jung, C. H., Jung, K. R., Lee, B. K., and Lee, K. W.: Wet scrubbing of polydisperse aerosols by freely falling droplets, J. Aerosol. Sci., 36, 1444-1458, 10.1016/j.jaerosci.2005.03.012, 2005.
Pitter, R. L., and Pruppacher, H. R.: A wind tunnel investigation of freezing of small water drops falling at terminal velocity in air, Quarterly Journal of the Royal Meteorological Society, 99, 540-550, 10.1002/qj.49709942111, 1973.

https://doi.org/10.5194/egusphere-2026-3946
Preprint. Discussion started: 28 July 2026

Pruppacher, H. R., and Klett, J. D.: Microphysics of Clouds and Precipitation, Atmospheric and Oceanographic Sciences Library, Kluwer Academic Publishers, Dordrecht, The Netherlands, 2010.
Rosky, E., Cantrell, W., Li, T., Nakamura, I., and Shaw, R. A.: Molecular simulations reveal that heterogeneous ice nucleation occurs at higher temperatures in water under capillary tension, Atmospheric Chemistry and Physics, 23, 10625-10642, 10.5194/acp-23-10625-2023, 2023.
Sax, R. I., and Goldsmith, P.: Nucleation of water drops by Brownian contact with AgI and other aerosols, Quarterly Journal of the Royal Meteorological Society, 98, 60-72, 10.1002/qj.49709841506, 1972.
Schaller, R. C., and Fukuta, N.: Ice Nucleation by Aerosol Particles: Experimental Studies Using a Wedge-Shaped Ice Thermal Diffusion Chamber, Journal of Atmospheric Sciences, 36, 1788-1802, 10.1175/1520-0469(1979)036<1788:INBAPE>2.0.CO;2, 1979.
Schiffman, Z. R., McMillan, K. A., Johnson, D. M., Gough, R. V., Davis, R. D., Brooks, S. D., and Tolbert, M. A.: Contact Freezing of Water Droplets by Crystalline Organic Acids, J Phys Chem A, 129, 7482-7495, 10.1021/acs.jpca.5c03258, 2025.
Schill, G. P., De Haan, D. O., and Tolbert, M. A.: Heterogeneous Ice Nucleation on Simulated Secondary Organic Aerosol, Environmental Science & Technology, 48, 1675-1682, 10.1021/es4046428, 2014.
Shaw, R. A., Durant, A. J., and Mi, Y.: Heterogeneous Surface Crystallization Observed in Undercooled Water, The Journal of Physical Chemistry B, 109, 9865-9868, 10.1021/jp0506336, 2005.
Slinn, W. G. N.: Some approximations for the wet and dry removal of particles and gases from the atmosphere, Water, Air, and Soil Pollution, 7, 513-543, 10.1007/BF00285550, 1977.
Svensson, E. A., Delval, C., von Hessberg, P., Johnson, M. S., and Pettersson, J. B. C.: Freezing of water droplets colliding with kaolinite particles, Atmospheric Chemistry and Physics, 9, 4295-4300, DOI 10.5194/acp-9-4295-2009, 2009.
Thompson, S. A., Peña, T. A., Chen, B., Sharma, M., Matthews, B. H., Li, R., Nowotarski, C. J., Rapp, A. D., and Brooks, S. D.: Variability in Ice Nucleating Particles Across Greater Houston Texas, Journal of Geophysical Research: Atmospheres, 130, 10.1029/2025jd044164, 2025.
Thornton, D. C. O., Brooks, S. D., Wilbourn, E. K., Mirrielees, J., Alsante, A. N., Gold-Bouchot, G., Whitesell, A., and McFadden, K.: Production of ice-nucleating particles (INPs) by fast-growing phytoplankton, Atmospheric Chemistry and Physics, 23, 12707-12729, 10.5194/acp-23-12707-2023, 2023.
Vali, G.: Supercooling of Water and Nucleation of Ice (Drop Freezer), American Journal of Physics, 39, 1125-1128, 1971.
Vali, G., DeMott, P. J., Möhler, O., and Whale, T. F.: Technical Note: A proposal for ice nucleation terminology, Atmos. Chem. Phys., 15, 10263-10270, 10.5194/acp-15-10263-2015, 2015.
Wang, C., Wu, J., Wang, H., and Zhang, Z.: Classical nucleation theory of ice nucleation: Second-order corrections to thermodynamic parameters, J Chem Phys, 154, 234503, 10.1063/5.0049570, 2021.
Wilson, E. B.: Probable Inference, the Law of Succession, and Statistical Inference, Journal of the American Statistical Association, 22, 209-212, 10.2307/2276774, 1927.
Yang, F., Cantrell, W. H., Kostinski, A. B., Shaw, R. A., and Vogelmann, A. M.: Is Contact Nucleation Caused by Pressure Perturbation?, Atmosphere, 11, 10.3390/atmos11010001, 2019.
Zhang, C., Wu, Z., Chen, J., Chen, J., Tang, L., Zhu, W., Pei, X., Chen, S., Tian, P., Guo, S., Zeng, L., Hu, M., and Kanji, Z. A.: Ice-nucleating particles from multiple aerosol sources in the urban environment of Beijing under mixed-phase cloud conditions, Atmospheric Chemistry and Physics, 22, 7539-7556, 10.5194/acp-22-7539-2022, 2022.
Zhang, Y., Subba, T., Matthews, B. H., Pettersen, C., Brooks, S. D., and Steiner, A. L.: Effects of Pollen on Hydrometeors and Precipitation in a Convective System, Journal of Geophysical Research: Atmospheres, 129, 10.1029/2023jd039891, 2024.